The Astrophysical Journal, 897:153 (9pp), 2020 July 10 https://doi.org/10.3847/1538-4357/ab97b8

Spicule Jets in the Solar Atmosphere Modeled with Resistive MHD and Thermal Conduction

J. J. González-Avilés[1,2], F. S. Guzmán[3], V. Fedun[4], and G. Verth[5]
[1] CONACYT—Servicio de Clima Espacial México—Laboratorio Nacional de Clima Espacial, SCiESMEX-LANCE, Morelia, Michoacán, México
jjgonzalez@igeofisica.unam.mx
[2] Instituto de Geofísica, Unidad Michoacán, Universidad Nacional Autónoma de México, Morelia, Michoacán, México
[3] Laboratorio de Inteligencia Artificial y Supercómputo. Instituto de Física y Matemáticas, Universidad Michoacana de San Nicolás de Hidalgo, Morelia, Michoacán, México
[4] Plasma Dynamics Group, Department of Automatic Control and Systems Engineering, University of Sheffield, Sheffield, S1 3JD, UK
[5] Plasma Dynamics Group, School of Mathematics and Statistics, University of Sheffield, Sheffield, S3 7RH, UK
Received 2020 March 21; revised 2020 May 27; accepted 2020 May 27; published 2020 July 14

Abstract

Using numerical simulations, we study the effects of magnetic resistivity and thermal conductivity in the dynamics and properties of solar jets with characteristics of Type II spicules and cool coronal jets. The dynamic evolution of the jets is governed by the resistive MHD equations with thermal conduction along the magnetic field lines on a 2.5D slice. The magnetic field configuration consists of two symmetric neighboring loops with opposite polarity, used to support reconnection and followed by the plasma jet formation. In total, 10 simulations were carried out with different values of resistivity and thermal conductivity that produce jets with different morphological and thermal properties we quantify. We find that an increase in magnetic resistivity does not produce significant effects on the morphology, velocity, and temperature of the jets. However, thermal conductivity affects both temperature and morphology of the jets. In particular, thermal conductivity causes jets to reach greater heights and increases the temperature of the jet-apex. Also, heat flux maps indicate the jet-apex and corona interchange energy more efficiently than the body of the jet. These results could potentially open a new avenue for plasma diagnostics in the Sun's atmosphere.

Unified Astronomy Thesaurus concepts: Solar physics (1476); Solar atmosphere (1477); Solar chromosphere (1479); Solar spicules (1525)

1. Introduction

Solar spicules are small-scale, jet-like plasma features observed ubiquitously in the solar chromosphere (Beckers 1972; Sterling 2000; De Pontieu et al. 2004, 2011). Spicules may play an important role in energy and material supply to the upper layers of the solar atmosphere (De Pontieu et al. 2011; Samanta et al. 2019). A number of theoretical models that related to formation and dynamics of spicules, including shocks wave plasma driving (Sterling 2000; De Pontieu et al. 2004), Alfvén waves (Cranmer & Woolsey 2015; Iijima & Yokoyama 2017), amplified magnetic tension (Martínez-Sykora et al. 2017b), or magnetic reconnection (Ding et al. 2011; Sheylag et al. 2018). Similarly, there are observations that highlight the evidence of magnetic reconnection in the generation of jets (Martínez Pillet et al. 2011; Borrero et al. 2013). In particular, Type II spicules are collimated jets that reach maximum heights of 3–9 Mm and even longer in coronal holes and have a typical lifetime of 50–150 s (De Pontieu et al. 2007b; Pereira et al. 2012), although these features can survive up to 500–800 s, while appearing and disappearing in multiple chromospheric passbands, due to thermal evolution (Pereira et al. 2014). Type II spicules show apparent upward motions with speeds of order 30–110 km s^{-1} and temperatures of order 10^4 K (Sterling 2000; Sterling et al. 2010). At the end of their life they usually exhibit rapid fading in chromospheric lines (De Pontieu et al. 2007a, 2017a).

Numerical modeling is an important way for styling and analyzing various dynamical plasma processes in the solar atmosphere. In particular, it is a powerful tool for better understanding of transient phenomena such as jets. For instance, Takasao et al. (2013), study the acceleration mechanism of chromospheric jets associated with emerging fluxes using 2D MHD simulations. Similarly, there are more sophisticated models of jet formation in 2D and 3D, which have been performed by Isobe et al. (2006), Pariat et al. (2009), Archontis et al. (2010), and Jiang et al. (2012a), that take into account physical effects such as magnetic resistivity and thermal conductivity. In particular, models including magnetic resistivity and thermal conductivity, are close to realistically describing the conditions in the solar atmosphere, as examples of this type of simulation reference Botha et al. (2011), where the authors use 3D MHD simulations to show that thermal conduction plays an essential role in the kink instability of coronal loops and cannot be ignored. Another example can be found in Fang et al. (2014), where the authors study the formation of coronal jets through the numerical simulation of the emergence of a twisted flux rope and found that field-aligned thermal conduction efficiently distributes the energy release, which is essential for comparing with synthetic emission. Apart from the ingredients of resistivity and thermal conductivity, there are other more sophisticated numerical simulations of Type II spicule formation that include the effect of radiation, partial ionization, and ambipolar diffusion (Martínez-Sykora et al. 2009, 2011, 2017a, 2017b; De Pontieu et al. 2017a).

In this paper we continue the analysis carried out by González-Avilés et al. (2017), by including the thermal conductivity flux

term in the resistive MHD equations, in addition to considering a wider range of resistivity values. In particular, we use a set of four realistic values of magnetic resistivity and thermal conductivity to analyze their effects on the morphology, maximum height, vertical velocity, thickness, temperature of the jet-apex, and lifetime of the jets modeled. Aside of state of the art contribution in simulations, like partial ionization, radiation, and ambipolar diffusion such as in De Pontieu et al. (2017a, 2017b), Nishizuka et al. (2008), Nóbrega-Siverio et al. (2016), Martínez-Sykora et al. (2012, 2017a, 2017b), Martínez-Sykora et al. (2018), and Yang et al. (2013), we show that thermal conductivity can modify the temperature, maximum height, and width of the jets with some characteristics of Type II spicules and cool coronal jets. Carrying out the study in 2.5D allows us to control computing time in a flexible way and in the use of various parameter combinations to analyze the numerical simulations.

The paper is organized as follows. In Section 2 we describe the resistive MHD equations with thermal conduction, the numerical methods we use, the model of solar atmosphere and the magnetic field configuration. In Section 3 we describe the parameters analyzed and the results of the numerical simulations for various experiments. Section 4 contains conclusions and final comments.

2. Model and Methods

2.1. The System of Resistive MHD Equations with Thermal Conduction

The model we consider to drive the plasma dynamics and the jet formation is the resistive MHD with thermal conduction and in particular we choose the Extended Generalized Lagrange Multiplier formulation (EGLM; Jiang et al. 2012b) to be effective at keeping the evolution of jets under control (González-Avilés et al. 2017, 2018). The system of equations we use for the evolution of the plasma is given in Jiang et al. (2012b), whose dimensionless version reads as follows:

$$\frac{\partial \rho}{\partial t} + \nabla \cdot (\rho \boldsymbol{v}) = 0, \tag{1}$$

$$\frac{\partial (\rho \boldsymbol{v})}{\partial t} + \nabla \cdot \left(\left(p + \frac{1}{2}\boldsymbol{B}^2 \right) \boldsymbol{I} + \rho \boldsymbol{v}\boldsymbol{v} - \boldsymbol{B}\boldsymbol{B} \right) = -(\nabla \cdot \boldsymbol{B})\boldsymbol{B} + \rho \boldsymbol{g}, \tag{2}$$

$$\frac{\partial E}{\partial t} + \nabla \cdot \left(\boldsymbol{v} \left(E + \frac{1}{2}\boldsymbol{B}^2 + p \right) - \boldsymbol{B}(\boldsymbol{B} \cdot \boldsymbol{v}) \right) = -\boldsymbol{B} \cdot (\nabla \psi) - \eta \nabla \cdot (\boldsymbol{J} \times \boldsymbol{B}) + \nabla \cdot \boldsymbol{q} + \rho \boldsymbol{g} \cdot \boldsymbol{v}, \tag{3}$$

$$\frac{\partial \boldsymbol{B}}{\partial t} + \nabla \cdot (\boldsymbol{B}\boldsymbol{v} - \boldsymbol{v}\boldsymbol{B} + \psi \boldsymbol{I}) = -\eta \nabla \times \boldsymbol{J}, \tag{4}$$

$$\frac{\partial \psi}{\partial t} + c_h^2 \nabla \cdot \boldsymbol{B} = -\frac{c_h^2}{c_p^2}\psi, \tag{5}$$

$$\boldsymbol{J} = \nabla \times \boldsymbol{B},$$

$$E = \frac{p}{(\gamma - 1)} + \frac{\rho \boldsymbol{v}^2}{2} + \frac{\boldsymbol{B}^2}{2},$$

where ρ is the mass density, $\boldsymbol{v}$ is the velocity field, $\boldsymbol{B}$ is the magnetic field, E is the total energy density, the plasma pressure p is described by the equation of state of an ideal gas $p = (\gamma - 1)\rho e$, where e is the internal energy and γ its adiabatic index, $\boldsymbol{g}$ is the gravitational field at the solar surface, $\boldsymbol{J}$ is the current density, η is the magnetic resistivity, and ψ is a scalar potential that helps to damp out the violation of the constraint $\nabla \cdot \boldsymbol{B} = 0$. Here c_h is a wave speed and c_p is the damping rate of the wave of the characteristic mode associated with ψ. In our simulations we use $c_p = \sqrt{c_r} c_h$, with $c_r = 0.18$ and $c_h = 0.001$, that have shown useful for 2.5D and 3D simulations.

The contribution of thermal conduction is included in the equation for the energy (3), through the heat flux vector that allows the heat propagation along the magnetic field lines (see, e.g., Jiang et al. 2012a)

$$\boldsymbol{q} = \kappa T^{5/2} (\boldsymbol{B} \cdot \nabla T) \boldsymbol{B} / B^2, \tag{6}$$

where κ is the thermal conductivity of the plasma, T is its temperature, and $\boldsymbol{B}$ is the magnetic field.

2.2. Numerical Methods

The evolution of jets is analyzed with a 2.5D approach, which consists of the restriction of the dynamics under consideration to have slab symmetry along one of the two horizontal directions of the spatial domain. We use Cartesian coordinates x and z describing the two-dimensional domain, and y is the direction of the slab symmetry.

We solve numerically the resistive EGLM-MHD equations with thermal conduction given by the system of Equations (1)–(5) using the Newtonian CAFE code (see, e.g., González-Avilés et al. 2015; González-Avilés & Guzmán 2018), on a uniform cell centered grid, using the method of lines with a third-order total variation diminishing Runge–Kutta time integrator described in Shu & Osher (1989). In order to use the method of lines, the right-hand side of Equations (1)–(5) are discretized using a finite volume approximation with High Resolution Shock Capturing methods, e.g., LeVeque (1992). For this, we first reconstruct the variables at cell interfaces using the minmod limiter, and numerical fluxes are calculated using the Harten–Lax–van Leer-Contact approximate Riemann solver (see, e.g., Li 2005).

2.3. Model of the Solar Atmosphere and Magnetic Field Configuration

At the initial time of the simulation, we assume the solar atmosphere to be in hydrostatic equilibrium, with the temperature field consistent with the semiempirical C7 model of the chromosphere transition region (Avrett & Loeser 2008). The density and temperature profiles used to start the simulations are shown at the top of Figure 1. For the equation of state we assume an adiabatic index $\gamma = 5/3$ and the gravitational field is set to $\boldsymbol{g} = -g\hat{z}$ with $g = 274\ \mathrm{m\ s^{-2}}$ in the equations of momentum and energy, more details can be found in González-Avilés et al. (2017).

The magnetic field configuration is a superposition of two neighboring loops and is constructed from a potential. Based on Priest (1982), Del Zanna et al. (2005), and González-Avilés et al. (2017), the magnetic field potential for two symmetric

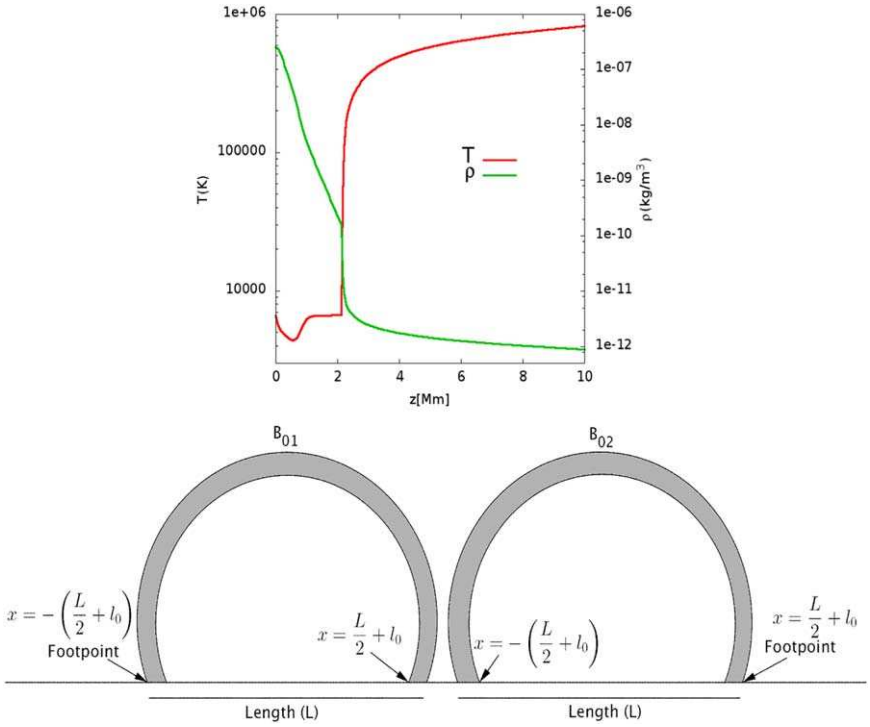

Figure 1. Top: temperature (red) and mass density (green) as a function of height for the C7 equilibrium solar atmosphere model. Bottom: two consecutive symmetric magnetic loop configurations with the same field strength $B_{01} = B_{02} = B_0$. These pictures were taken from González-Avilés et al. (2017).

loops, that decreases with height exponentially, is given by

$$A_y(x, z) = \frac{B_0}{k}(\cos(k(x + l_0)) + \cos(k(x - l_0)))\exp(-kz), \quad (7)$$

where l_0 parameterizes the position of the foot points for each of the loops and B_0 is the magnetic field strength. In this paper, we use the parameters $B_0 = 40$ G and $l_0 = 3.5$ Mm, because they are physically sound and produce jets with some properties of Type II spicules successfully (González-Avilés et al. 2017). In this manner we concentrate on the properties of the ejected structure. A schematic picture of the magnetic configuration is shown to the bottom of Figure 1.

Further details of the set up are that we fix $k = \pi/L$ with $L = 8$ Mm, where L is the distance between the two foot points of the loop. Then we execute simulations in the 2D domain $x \in [-4, 4] \times z \in [0, 10]$ in units of Mm, covered with 300×375 grid cells in x and z direction correspondingly. Since we are using a three-dimensional code, we cover the additional direction y with four cells. The boundary conditions used are outflow at all faces of the domain.

3. Results of Numerical Simulations and Analysis

3.1. Parameters Analyzed

We study the effects of magnetic resistivity and thermal conductivity on the jet formation process with characteristics of Type II spicules. The following parameters were analyzed in detail for different runs: the maximum height, width of jet-apex, average temperature of the jet-apex at maximum height and time when the jet reaches the maximum height obtained with the various combinations of the resistivity η and thermal conductivity κ.

Table 1
Values of η and κ Used in Our Study

Run #	η	κ	h_{max} (Mm)	Width (Mm)	T_{head} (K)	t_{hmax} (s)
1	**3.97e-8**	**0**	**7.3**	**1.1**	**56240**	**210**
2	8e-8	0	7.3	1.1	57269	210
3	1.6e-7	0	7.3	1.1	56678	210
4	2.5e-7	0	7.3	1.1	58643	210
5	3.97e-8	2500	7.5	0.92	62485	210
6	**3.97e-8**	**3275**	**7.5**	**0.92**	**63920**	**210**
7	3.97e-8	29479	7.7	0.82	69118	210
8	3.97e-8	32755	7.7	0.82	73049	210
9	8e-8	2500	7.5	0.92	55395	210
10	**8e-8**	**32755**	**7.7**	**0.82**	**61714**	**210**

Note. For each case we list the following properties of the simulated jet: maximum height, width of the jet-apex at h_{max}, average of temperature of the jet-apex at h_{max}, and time when the jet reaches the maximum height.

With the various combinations of these parameter values we define 10 cases specified in Table 1, the combinations were chosen taking into account the level of realism of the values. For ease, in what follows, we will use the code unit values of resistivity and thermal conductivity to define and describe the various scenarios in our analysis.

For resistivity we use the values $\eta = 5 \times 10^{-2}$, 1×10^{-1}, 2×10^{-1}, $3 \times 10^{-1}\Omega \cdot$ m, which are reasonable values for a fully ionized solar atmosphere (Priest 2014). For thermal conductivity we use the values $\kappa = 0$, 7.6×10^{-13}, 10^{-12}, 9×10^{-12}, 10^{-11} W m^{-1} K$^{-7/2}$, where 10^{-11} W m^{-1} K$^{-7/2}$ is a typical value in the chromosphere and 9×10^{-12} W m^{-1} K$^{-7/2}$ is a typical value in the corona for a fully ionized gas (Spitzer 1962; Botha et al. 2011). We consider the fully ionized condition to be acceptable due to the timescales of the jet

processes obtained in this paper. For example, at the chromospheric level, the timescale of neutron-ion collision frequency lies between 1–10^4 Hz (see, e.g., Figure 4 of Martínez-Sykora et al. 2012), which is a timescale at least one order of magnitude smaller than that of the jet evolution shown in our simulations. With respect to thermal conductivity, we use values that range from those suitable for the chromosphere for a partially ionized plasma, up to those appropriate for the fully ionized plasma at the corona (see, e.g., Spitzer 1962; Botha et al. 2011). Following the conventions of González-Avilés & Guzmán (2015) to make the MHD equations dimensionless, we obtain the dimensionless values of $\bar{\eta}$ and $\bar{\kappa}$ according to the following scaling:

$$\bar{\eta} = \frac{\eta}{L_0 \mu_0 v_0}, \tag{8}$$

$$\bar{\kappa} = \frac{\kappa T_0^{7/2}}{L_0 \rho_0 v_0^3}, \tag{9}$$

where $L_0 = 10^6$ m, $\mu_0 = 4\pi \times 10^{-7}$, $v_0 = 10^6 \mathrm{m}\, s^{-1}$, $\rho_0 = 1 \times 10^{-12}$ kg m^{-3}, and $T_0 = 7.269 \times 10^7$ K. Therefore, the values in code units for resistivity and thermal conductivity constants are $\eta = 3.97 \times 10^{-8}$, 8×10^{-8}, 1.6×10^{-7}, 2.5×10^{-7}, and $\kappa = 0, 2500, 3275, 29479, 32755$.

3.2. Results of Numerical Simulations

Of all the runs for simulations summarized in Table 1, we select three illustrative ones, e.g., Run #1: $\eta = 3.97 \times 10^{-8}$, $\kappa = 0$, Run #6: $\eta = 3.97 \times 10^{-8}$, $\kappa = 3275$, and Run #10: $\eta = 8 \times 10^{-8}$, $\kappa = 32{,}755$, which are highlighted in bold. In Figure 2 we show snapshots of the temperature, vertical velocity with the vector field distribution and the magnitude of the heat flux $|\boldsymbol{q}|$ given by Equation (6) with magnetic field lines at time $t = 210$ s for the three illustrative Runs. For example, in Figures 2(a)–(c) we show the results for the values $\eta = 3.97 \times 10^{-8}$ and $\kappa = 0$, which are practically the same snapshots corresponding to the top of Figure 3 of González-Avilés et al. (2017), these snapshots will be useful for comparison with cases where thermal conductivity is included. Figure 2(c) shows the magnetic field lines with $|\boldsymbol{q}| = 0$, corresponding to $\kappa = 0$, for completeness.

In Figures 2(d)–(f) we show the results for Run #6, with the combination of parameters $\eta = 3.97 \times 10^{-8}$ and $\kappa = 3275$. In this case according to the temperature map, we can see that the jet is wider in its lower part and thinner in the upper part just below its apex compared to the Run #1, and reaches a height of 7.5 Mm, which represents 0.2 Mm larger than the jet of Run #1. In addition, the vertical velocity is higher at the sides of the jet compared to that of Run #1. The magnitude of the heat flux $|\boldsymbol{q}|$ is high at the top of the jet-apex, and at the sides beneath the jet-apex, while inside the jet structure the value tends to zero. The reason is that $\boldsymbol{q}$ is basically a projection of ∇T along the field lines, then it is maximum when ∇T is large and has an important component parallel to field lines. At the top of jet-apex the gradient of temperature is nearly radial (i.e., perpendicular to the ball shape of the jet-apex) as seen in Figure 2(a) and magnetic field lines have a radial component; another case is that heat flux is nearly zero aside the jet for z between 2 and 7 Mm because the gradient of T is nearly horizontal whereas the magnetic field lines are nearly vertical, and therefore the effect of thermal conductivity is minimal.

In Figures 2(g)–(i) we show the results for Run #10 with values $\eta = 8 \times 10^{-8}$ and $\kappa = 32{,}755$, which is a combination that includes the highest value of thermal conductivity. In this case we can also see that the bottom of the jet is about 0.1 Mm wider than the bottom of the jet of Run #1 and jet-apex is 0.28 Mm thinner compared to the Run #1, and 0.10 Mm thinner compared to the Run #6. This jet reaches a height of about 7.7 Mm, which is 0.4 Mm higher compared to Run #1 and 0.2 Mm higher compared to Run #6, and in the same way it is seen that the vertical speed is greater aside the jet. In Figure 2(i), $|\boldsymbol{q}|$ is higher at the top of the jet, similar to Figure 2(f); however, in this case $|\boldsymbol{q}|$ reaches higher values, which correspond with bigger κ used in this numerical run. The jet during development reaches maximum speeds of the order of 100 km s^{-1} at early times, between 0 and 50 s, while at later times after 60 s the speed decreases to values up to 15–30 km s^{-1}. Therefore in the first stage of the jet's evolution the speeds are comparable to those of Type II spicules, whereas at later times the speeds are smaller than the lower limit of the observed velocities. Similarly, the vertical speed of our jets have similarities with the observed velocities of the Rapid Redshifted and Blueshifted Excursions (RREs, RBEs), which are in the range of 50–150 km s^{-1} (Langangen et al. 2008). In addition, the vector field shows the appearance of vorticity near the top of the jets. According to the results reported in Table 1, the width of the jet-apex at the maximum height vary in the range 0.8–1.1 Mm, which is four times greater than the width of 0.25 Mm that has been observed in RRE and RBE spicule features (Kuridze et al. 2015); however, the widths of the RREs and RBEs are of the entire observed structure. In fact, if we estimate the width of the jet structure from our simulations, we obtain that the width varies in the range 0.2–0.6 Mm from the bottom of the jet to below its apex, these widths are close to the observed values. Regarding the spicules observed at the limb, cross-sectional widths have been estimated in the range 0.27–0.36 Mm (Sharma et al. 2018), which are again smaller than the width of the jet-apex, but they are close to the widths estimated in the entire jet structure of our simulations. Similarly to the results obtained in González-Avilés et al. (2017), in this paper we find that jets show a special feature at the apex with a bulb possibly related to the formation of a Kelvin–Helmholtz (KH) type of instability. However, as was shown in González-Avilés et al. (2017), this instability is suppressed by the magnetic field.

To see more clearly the differences in morphology for the cases shown in Figure 2, in Figure 3 we show a zoom of snapshots of temperature and vertical velocity v_z together with the velocity field, magnitude of the heat flux $|\boldsymbol{q}|$ with magnetic field lines, and the y-component of the vorticity $(\nabla \times \boldsymbol{v})_y$ with the velocity field at the time when the jets are at the same height. For example, in Figures 3(a)–(c) we can see that the jets have different morphology when they are at the same height, in particular the jet with the highest value of thermal conductivity is smaller and thinner. The cold material develops a horizontal structure connected to the jet-apex that is more notorious for higher κ, which can also be seen in Figure 2. In Figures 3(d)–(f) we show that the vertical component of velocity is higher on the side of the jet for the cases when thermal conductivity is higher. In Figure 3(g), we show the case of Run #1 when $|\boldsymbol{q}|$ is zero. The magnetic field lines have the shape of the jet shown in Figure 2(a). In Figures 3(h) and (i) we show that $|\boldsymbol{q}|$ is high near the top of the jet-apex for Runs #6 and #10, where the

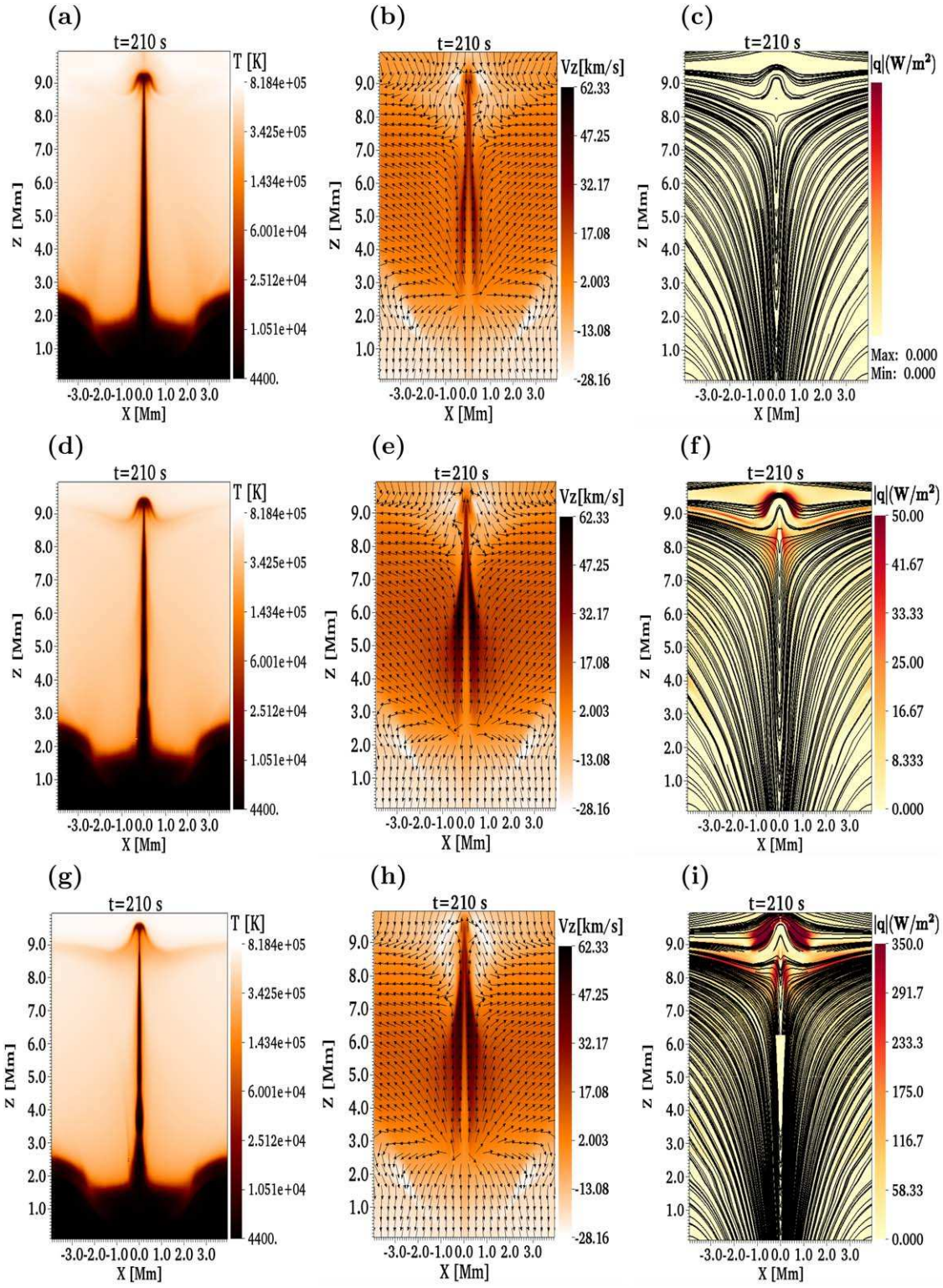

Figure 2. From left to right we show snapshots of (i) temperature in kelvin, (ii) the vertical component of velocity (v_z km s^{-1}), where the arrows show the velocity field and (iii) the magnitude of the heat flux $|\boldsymbol{q}|$ in W m^{-2} with magnetic field lines. In panels (a), (b), and (c) we show the results for Run #1 ($\eta = 3.97 \times 10^{-8}$ and $\kappa = 0$) at time $t = 210$ s. In panels (d), (e), and (f) we show the results for the Run #6 ($\eta = 3.97 \times 10^{-8}$ and $\kappa = 3275$) at time $t = 210$ s. Finally, in panels (g), (h), and (i), we show the results for Run #10 ($\eta = 8 \times 10^{-8}$ and $\kappa = 32{,}755$) at time $t = 210$ s. Note that as the value of thermal conductivity increases the jet gets thinner closer to the observations. In this figure we only show temperature maps, but the mass density has the same morphology. Heat flux is particularly consistent, notice it is nearly zero at the body of the jet where ∇T is perpendicular to the field lines, and becomes important at the top of the jet, where ∇T is more parallel to the shape of the jet-apex and field lines nearly horizontal. It is also seen that heat transfer produces a stream of cold material from the jet-apex to the sides. We use different density of magnetic field lines in each case, to capture some of the differences, specially at the jet-apex.

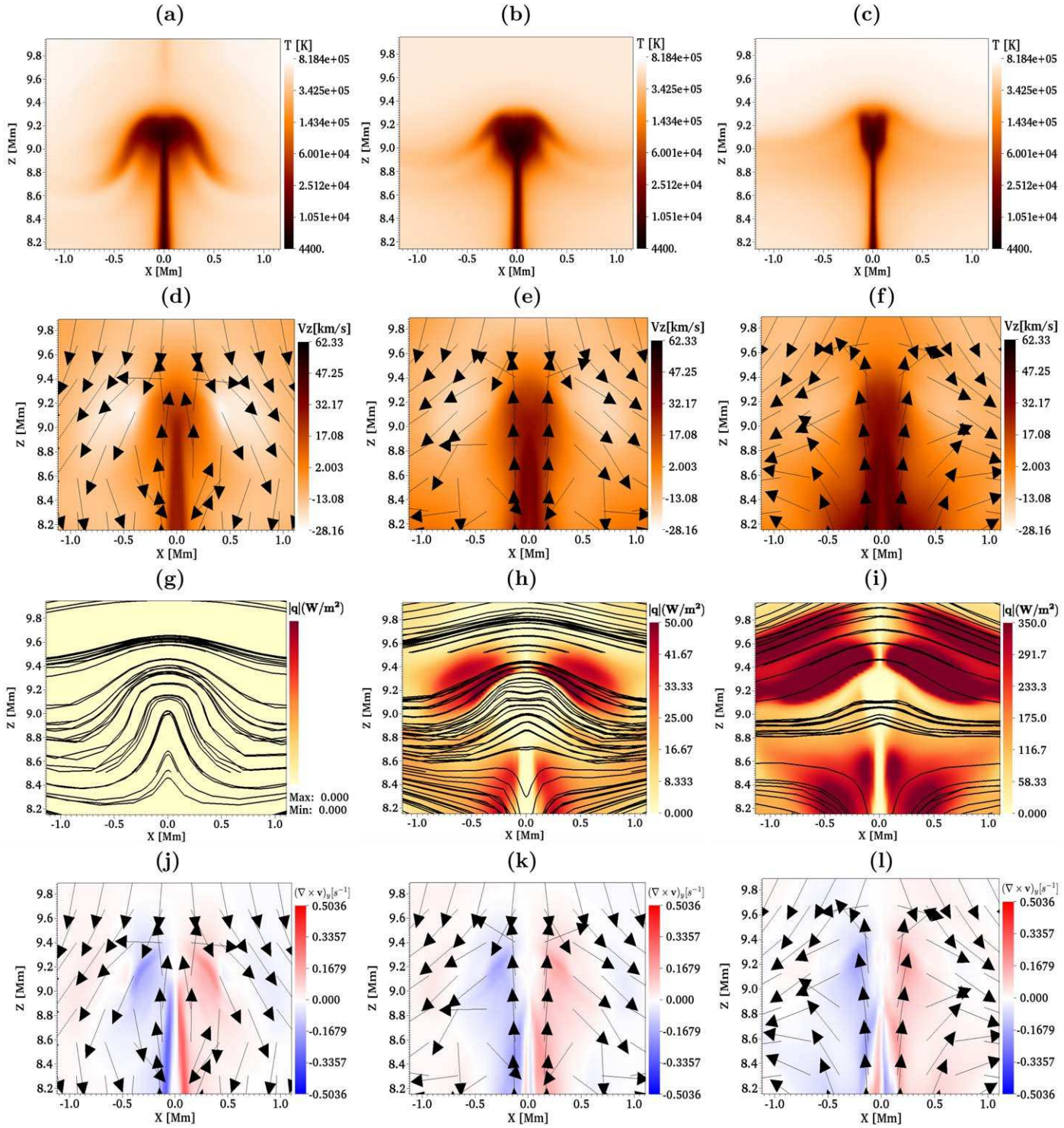

Figure 3. From left to right we show a zoom of the region around the jets for Runs #1, Run #6, and Run #10. We show the temperature in kelvin (panels (a), (b), and (c)), vertical component of velocity v_z in km s^{-1} with the velocity vector field shown as black arrows (panels (d), (e), and (f)), magnitude of the heat flux $|\boldsymbol{q}|$ in W m^{-2} as well as magnetic field lines (panels (g), (h), and (i)) and y-component of vorticity $(\nabla \times \boldsymbol{v})_y$ in s^{-1} (panels (j), (k), and (l)). Note that we only show the temperature, but the mass density has the same morphology. In all the figures the snapshot is taken when the jet is at the same height.

magnetic field lines have a significant horizontal component. We can also see that the magnetic field lines follow the jet structure in Run #1, whereas for the other two cases the magnetic field lines tend to flatten near the jet-apex. This is consistent with the fact that $\beta < 1$ outside the jet and $\beta > 1$ inside, where hydrodynamical effects dominate. Finally, in Figures 3(j)–(l) we can notice that at the sides of the jet-apex, the flux develops vorticity, which apparently does not change with the increase in thermal conductivity. The appearance of the vorticity could be due to the interaction of the cold gas with the hotter plasma in the corona.

In order to quantify the influence of resistivity and thermal conductivity, we average the temperature and vertical velocity along the jet and show them as functions of time. We also

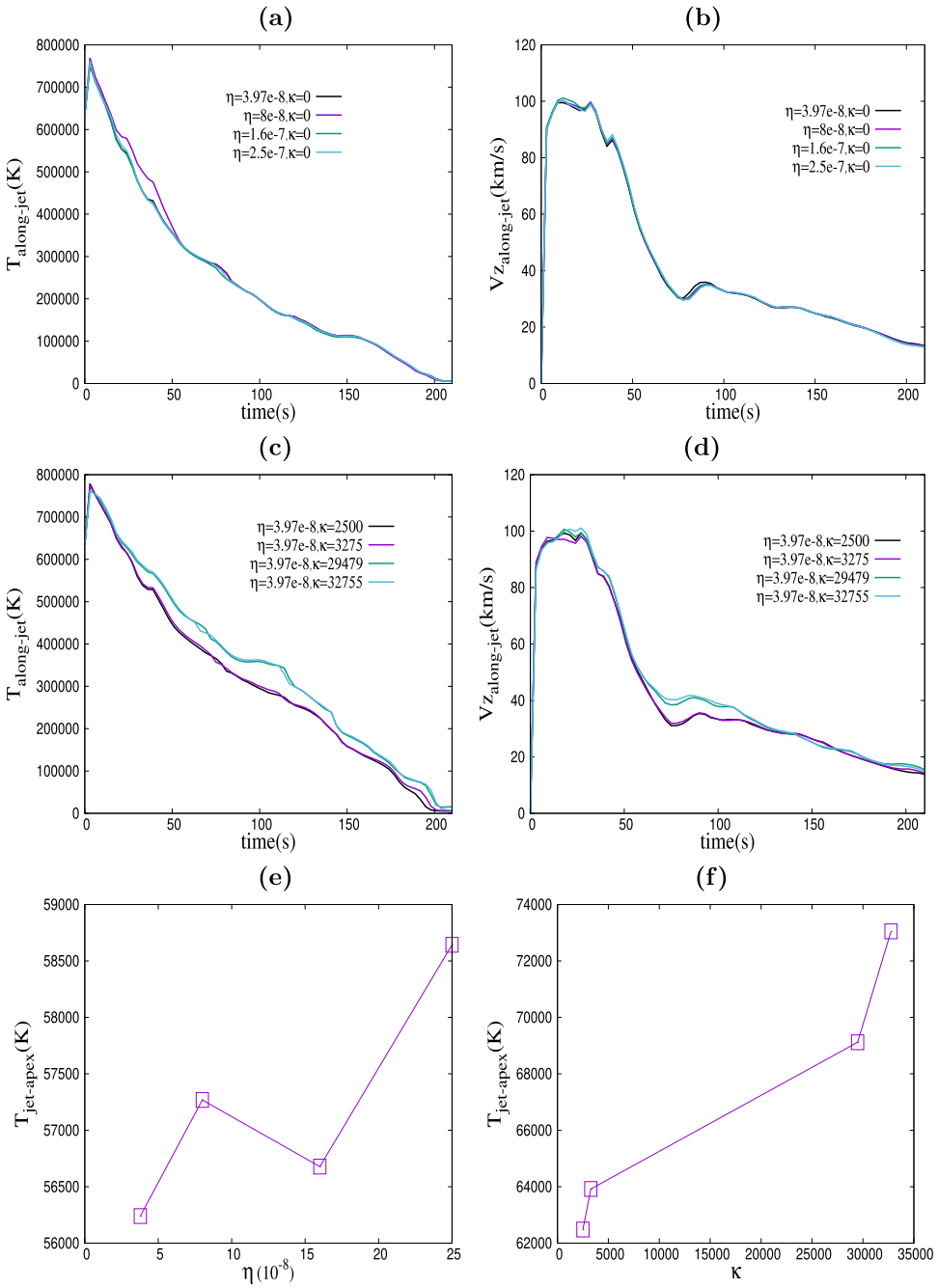

Figure 4. Panel (a): temperature along the jet $T_{\text{along-jet}}$ in kelvin as a function of time for different values of η and $\kappa = 0$. Panel (b): vertical velocity v_z along the jet in kilometers per second as a function of time for different values of η and $\kappa = 0$. Panel (c): temperature along the jet $T_{\text{along-jet}}$ in kelvin as a function of time for different values of κ and $\eta = 3.97 \times 10^{-8}$. Panel (d): vertical velocity v_z along the jet in kilometers per second as a function of time for different values of κ and $\eta = 3.97 \times 10^{-8}$. Panel (e): average jet-apex temperature T_{head} as a function of the η at time $t = 210$ s. Panel (f): average jet-apex temperature T_{head} as a function of κ at time $t = 210$ s.

calculate an average of the jet-apex temperature at time $t = 210$ s. For instance, in Figure 4(a), we show the temperature along the jet as a function of time for different values of η and $\kappa = 0$. In this case, we notice that temperature does not show significant variations in all cases. For example, in Figure 4(b) we have found that vertical velocity along the jet is less sensitive to the increase of resistivity. In Figure 4(c), we show the temperature along the jet as a function of time for different values of κ and $\eta = 3.97 \times 10^{-8}$. In this case, we can see that the temperature increases slightly when the value of the thermal conductivity is higher. In Figure 4(d), we show that the vertical component of velocity along the jet is higher about time $t \sim 100$ s when the value of κ is higher, for all other times the velocity remains without significant variations. In Figures 4(b) and (d), we can see that the vertical velocity along the jet shows a bump about the time $t \sim 100$ s; this is due to the rapid acceleration of the plasma produced by magnetic reconnection, which is triggered by the magnetic loops close together with opposite polarity and the inclusion of resistivity as indicated in González-Avilés et al. (2017). In Figure 4(e), we show the average of jet-apex temperature as a function of η for $\kappa = 0$ at time $t = 210$ s. For the values of η used, the

temperature increases by 2.1%. Finally, in Figure 4(f), we show the average of jet-apex temperature as a function of κ and $\eta = 3.97 \times 10^{-8}$. In this case we can see that temperature of the jet-apex increases by ∼8.1% with respect to the temperature obtained with the smallest value of conductivity.

4. Conclusion and Final Comments

In this paper we perform numerical simulations to explore the effects of magnetic resistivity and thermal conductivity in the dynamics and parameters of jet structures with some characteristics of Type II spicules. This paper is a continuation of the work presented in González-Avilés et al. (2017), where we show that jets with features of Type II spicules and cool coronal jets can be formed as a result of magnetic reconnection in a scenario with magnetic resistivity.

According to the analysis carried out in this paper, we found that the inclusion of thermal conductivity along the magnetic field lines affects the morphology of the jets; in particular, the combination $\kappa = 32{,}755$ and $\eta = 8 \times 10^{-8}$ makes the jet structure 0.1 Mm wider at its lower part and 0.28 Mm thinner at its apex, measured with respect to jets where only resistivity is considered. In addition, the increase in thermal conductivity makes the jets reach maximum heights of about 7.7 Mm, such heights are 0.4 Mm larger compared to jets with only resistivity. According to the results of the Runs #5 to #8 shown in Table 1, we can see that an increase of the order of 10 times the value of thermal conductivity causes the jet to reach a maximum height 0.2 Mm larger, it also makes the jet-apex 0.28 Mm thinner, this means that the inclusion of thermal conductivity makes the jets have a width closer to the value of observations. One of the most important results is that the jet-apex heat up and reach temperatures of the order of 73,000 K for the combination $\eta = 3.97 \times 10^{-8}$ and $\kappa = 32{,}755$ in comparison with the combination $\eta = 3.97 \times 10^{-8}$ and $\kappa = 0$, in which the jet-apex temperature is of the order 58,000 K. These results are similar to those obtained in Kuźma et al. (2017); however, in this paper the formation and evolution of solar spicules use numerical simulations triggered with a vertical velocity pulse that is launched from the upper chromosphere. Instead, in our analysis, we do not perturb the solar atmosphere with any pulse at the initial time, rather it is the magnetic reconnection that accelerates the plasma and forms the jet. Another difference is that we use a range of resistivity and thermal conductivity values consistent with a fully ionized solar atmosphere.

We have also found that the increase in the resistivity does not affect the morphology of the jets, and although it slightly increases the jet-apex temperature it was found that it does not modify the behavior of the temperature along the whole jet structure.

Note that although the model of two magnetic loops close together with opposite polarity is very simple and approximate, this configuration can support the formation of jets mimicking some properties of Type II spicules and cool coronal jets. Furthermore, the inclusion of resistivity and thermal conductivity is consistent with the physical properties found in the solar atmosphere. In particular, the resistivity supports development of the magnetic reconnection process, and thermal conductivity helps the heat to propagate more efficiently along the magnetic field lines.

These results are important to understanding of nature of spicules. The reason is that two different values of thermal conductivity produce spicules with different temperature and maximum height. From the other side, the problem could be degenerate, because two jets with the same temperature and height could be obtained with and without thermal conductivity at the price of modifying, for example, the magnetic field, or the temperature model of the chromosphere-corona interface. Eventually the addition of ingredients to a model-simulation will have to face the observational restrictions that will in turn refine the parameter values of simulations and the degeneracy of the problem can be an important problem in itself. Finally, it is important to mention the role of heat transfer prior to jet propagation, in this case the timescale of the physical process related to the thermal conductivity is much smaller than the time needed for jet development and to reach the maximum height. At the beginning of the simulation runs, the temperature gradient has its maximum value at the interface, and at the same time the field lines are nearly parallel to this gradient near the foot points, therefore heat transfer influences the initial numerical background in terms of temperature changes even before the jet propagates up. This is an important factor that deserves special attention.

This research is partly supported by the following grants: Newton Fund, Royal Society-Newton Mobility grant NI160149, CIC-UMSNH 4.9, and CONACYT 258726 (Fondo Sectorial de Investigación para la Eduación). The simulations were carried out in the facilities of the Big Mamma cluster at the LIASC-IFM and in the cluster of the CESCOM-UNAM. V.F. and G.V. thank the STFC for their financial support, grant No. ST/M000826/1. V.F. would like to thank the International Space Science Institute (ISSI) in Bern, Switzerland, for the hospitality provided to the members of the team "The Nature and Physics of Vortex Flows in Solar Plasmas." J.J.G.A. thanks Cátedras CONACYT (CONACYT Fellow) for supporting this work. Space Weather Service Mexico (SCiESMEX) is sponsored by the Catedras-CONACYT Program, project 1045. Visualization of the simulation's data was done with the use of the VisIt software package (Childs et al. 2012). This research has received financial support from the European Union's Horizon 2020 research and innovation program under grant agreement No. 824135 (SOLARNET).

ORCID iDs

J. J. González-Avilés https://orcid.org/0000-0003-0150-9418
F. S. Guzmán https://orcid.org/0000-0002-1350-3673
V. Fedun https://orcid.org/0000-0002-0893-7346
G. Verth https://orcid.org/0000-0002-9546-2368

References

Archontis, V., Tsinganos, K., & Gontikakis, C. 2010, A&A, 512, L2
Avrett, E. H., & Loeser, R. 2008, ApJS, 175, 229
Beckers, J. M. 1972, ARA&A, 10, 73
Borrero, J. M., Martínez Pillet, V., Schmidt, W., et al. 2013, ApJ, 768, 69
Botha, G. J. J., Arber, T. D., & Hood, A. W. 2011, A&A, 525, A96
Childs, H., Brugger, E., Whitlock, B., et al. 2012, High Performance Visualization: Enabling Extreme-Scale Scientific Insight, 357-372 (London/Boca Raton, FL: Chapman and Hall/CRC press)
Cranmer, S. R., & Woolsey, L. N. 2015, ApJ, 812, 71
De Pontieu, B., De Moortel, I., Martínez-Sykora, J., & McIntosh, S. W. 2017a, ApJL, 845, L18
De Pontieu, B., Erdélyi, R., & James, S. P. 2004, Natur, 430, 536
De Pontieu, B., McIntosh, S., & Hansteen, V. H. 2007b, PASJ, 59, 655

De Pontieu, B., McIntosh, S., Martínez-Sykora, J., Peter, H., & Pereira, T. M. D. 2017b, ApJL, 799, L12
De Pontieu, B., McIntosh, S. W., Carlsson, M., et al. 2007a, Sci, 318, 1574
De Pontieu, B., McIntosh, S. W., Carlsson, M., et al. 2011, Sci, 331, 55
Del Zanna, L., Schaekens, E., & Velli, M. 2005, A&A, 431, 1095
Ding, J. Y., Madjarska, M. S., Doyle, J. G., et al. 2011, A&A, 535, A95
Fang, F., Fang, Y., & McIntosh, S. W. 2014, ApJL, 789, L19
González-Avilés, J. J., Cruz-Osorio, A., Lora-Clavijo, F. D., & Guzmán, F. S. 2015, MNRAS, 454, 1871
González-Avilés, J. J., & Guzmán, F. S. 2015, MNRAS, 451, 300
González-Avilés, J. J., & Guzmán, F. S. 2018, ITPS, 46, 2378
González-Avilés, J. J., Guzmán, F. S., & Fedun, V. 2017, ApJ, 836, 24
González-Avilés, J. J., Guzmán, F. S., Fedun, V., et al. 2018, ApJ, 856, 176
Iijima, H., & Yokoyama, T. 2017, ApJ, 848, 38
Isobe, H., Miyagoshi, T., Shibata, K., & Yokoyama, T. 2006, PASJ, 58, 423
Jiang, R.-L., Fang, C., & Chen, P.-F. 2012a, ApJ, 751, 152
Jiang, R.-L., Fang, C., & Chen, P.-F. 2012b, CoPhC, 183, 1617
Kuridze, D., Henriques, V., Mathioudakis, M., et al. 2015, ApJ, 802, 26
Kuźma, B., Murawski, K., Zaqarashvili, T. V., Konkol, P., & Mignone, P. 2017, A&A, 597, A133
Langangen, Ø., De Pontieu, B., Carlsson, M., et al. 2008, ApJL, 679, L167
LeVeque, R. J. 1992, Numerical Methods for Conservations Laws (Basel: Birkhauser)
Li, S. 2005, JCoPh, 203, 344
Martínez Pillet, V., del Toro Iniesta, J. C., & Quintero Noda, C. 2011, A&A, 530, A111
Martínez-Sykora, J., De Pontieu, B., Carlsson, M., et al. 2017a, ApJ, 847, 36
Martínez-Sykora, J., De Pontieu, B., De Moortel, I., Hansteen, V. H., & Carlsson, M. 2018, ApJ, 860, 116
Martínez-Sykora, J., De Pontieu, B., & Hansteen, V. 2012, ApJ, 753, 161
Martínez-Sykora, J., De Pontieu, B., Hansteen, V. H., et al. 2017b, Sci, 356, 1269
Martínez-Sykora, J., Hansteen, V., De Pontieu, B., & Carlsson, M. 2009, ApJ, 701, 1569
Martínez-Sykora, J., Hansteen, V., & Moreno-Insertis, F. 2011, ApJ, 736, 9
Nishizuka, N., Shimizu, M., Nakamura, T., et al. 2008, ApJL, 683, L83
Nóbrega-Siverio, D., Moreno-Insertis, F., & Martínez-Sykora, J. 2016, ApJ, 822, 18
Pariat, E., Antiochos, S. K., & DeVore, R. C. 2009, ApJ, 691, 61
Pereira, T. M. D., De Pontieu, B., & Carlsson, M. 2012, ApJ, 759, 18
Pereira, T. M. D., De Pontieu, B., Carlsson, M., et al. 2014, ApJL, 792, L15
Priest, E. R. 1982, Solar Magnetohydrodynamics (Dordrecht: Reidel)
Priest, E. R. 2014, Magnetohydrodynamics of the Sun (Cambridge: Cambridge Univ. Press)
Samanta, T., Tian, H., Yurchyshyn, V., et al. 2019, Sci, 366, 890
Sharma, R., Verth, G., & Erdélyi, R. 2018, ApJ, 853, 61
Sheylag, S., Litvinenko, Y. E., Fedun, V., et al. 2018, A&A, 620, A159
Shu, C. W., & Osher, S. J. 1989, JCoPh, 83, 32
Spitzer, L. 1962, Physics of Fully Ionized Gases (New York: Interscience)
Sterling, A. C. 2000, SoPh, 196, 79
Sterling, A. C., Harra, L. K., & Moore, R. L. 2010, ApJ, 722, 1644
Takasao, S., Isobe, H., & Shibata, K. 2013, PASJ, 65, 62
Yang, L., He, J., Peter, H., et al. 2013, ApJ, 777, 16